

## Statistical analysis of kinetic energy entrainment in a model wind turbine array boundary layer

Nicholas Hamilton, Hyung Suk Kang, Charles Meneveau, and Raúl Bayoán Cal

Citation: [Journal of Renewable and Sustainable Energy](#) 4, 063105 (2012); doi: 10.1063/1.4761921

View online: <http://dx.doi.org/10.1063/1.4761921>

View Table of Contents: <http://scitation.aip.org/content/aip/journal/jrse/4/6?ver=pdfcov>

Published by the [AIP Publishing](#)

---

An advertisement for physiciststodayJOBS. On the left is a photograph of a man in a dark suit and striped tie, looking surprised with his mouth open and one hand cupped behind his ear. To the right of the photo, the text 'HAVE YOU HEARD?' is written in large, bold, dark red capital letters. Below this, in smaller dark red text, is 'Employers hiring scientists and engineers trust'. Underneath that, 'physicstodayJOBS' is written in a blue, sans-serif font. At the bottom right is a square QR code. Below the QR code, the URL 'http://careers.physicstoday.org/post.cfm' is written in a small, black, sans-serif font.

**HAVE YOU HEARD?**

Employers hiring scientists  
and engineers trust  
**physicstodayJOBS**

<http://careers.physicstoday.org/post.cfm>

## Statistical analysis of kinetic energy entrainment in a model wind turbine array boundary layer

Nicholas Hamilton,<sup>1</sup> Hyung Suk Kang,<sup>2</sup> Charles Meneveau,<sup>3</sup>  
and Raúl Bayoán Cal<sup>1</sup>

<sup>1</sup>*Department of Mechanical and Materials Engineering, Portland State University, Portland, Oregon 97207, USA*

<sup>2</sup>*Department of Mechanical Engineering, Johns Hopkins University, Baltimore, Maryland 21218, USA*

<sup>3</sup>*Department of Mechanical Engineering & CEA FM, Johns Hopkins University, Baltimore, Maryland 21218, USA*

(Received 1 May 2012; accepted 14 September 2012; published online 12 November 2012)

For large wind farms, kinetic energy must be entrained from the flow above the wind turbines to replenish wakes and enable power extraction in the array. Various statistical features of turbulence causing vertical entrainment of mean-flow kinetic energy are studied using hot-wire velocimetry data taken in a model wind farm in a scaled wind tunnel experiment. Conditional statistics and spectral decompositions are employed to characterize the most relevant turbulent flow structures and determine their length-scales. Sweep and ejection events are shown to be the largest contributors to the vertical kinetic energy flux, although their relative contribution depends upon the location in the wake. Sweeps are shown to be dominant in the region above the wind turbine array. A spectral analysis of the data shows that large scales of the flow, about the size of the rotor diameter in length or larger, dominate the vertical entrainment. The flow is less incoherent below the array, causing decreased vertical fluxes there. The results show that improving the rate of vertical kinetic energy entrainment into wind turbine arrays is a standing challenge and would require modifying the large-scale structures of the flow. Such an optimization would in the future aid recovery of the wind turbine wake towards conditions corresponding to the undisturbed atmospheric boundary layer. © 2012 American Institute of Physics. [<http://dx.doi.org/10.1063/1.4761921>]

### I. INTRODUCTION

The advent of wind energy as a significant contributor to the global energy supply has raised interest in the characteristics of very large arrays of wind turbines. In the analysis of a single, or a small number of turbines, the horizontal flux of kinetic energy is often considered. And wake spreading and downstream recovery play an important role. Wakes of single wind turbines have been characterized extensively in the past, see, e.g., Refs. 5–7. Vermeer *et al.* performed a survey of available experimental and numerical data in both the near and far wake regions, showing saturation of turbulence after only several rows of turbines. They also show that energy spectra shift away from larger, more energetic scales toward higher frequency fluctuations. Porté-Agel and Chamorro<sup>8</sup> studied the effects of surface roughness on the wake area and flow characteristics, demonstrating the sensitivity of turbine wakes to environmental parameters and inflow conditions of the atmospheric boundary layer.

As larger arrays are being considered, they approach the asymptotic limit of what has become known as the “infinite wind farm” (Refs. 1 and 2), involving a flow regime that can be denoted as the “fully developed wind turbine array boundary layer” (Ref. 3). Within this regime, the entirety of the flux of kinetic energy available at the wind turbine locations must be entrained from the layers above (vertical entrainment), since no spatial evolution occurs along the horizontal direction, on average. Vertical entrainment of kinetic energy has been recently

quantified in wind tunnel experiments (Ref. 4) and large eddy simulation (Refs. 3 and 16). These data show that vertical transport of kinetic energy due to turbulence dominates the budget of kinetic energy rather than horizontal differences between flux of mean kinetic energy. Additionally, a model has been proposed furthering the work of Refs. 1 and 2 that includes atmospheric stratification.<sup>46</sup> The model uses a simplified stability correction function,  $\phi_m$  to modify the mixing length of the turbulence both below and above the wind turbines, including effects of thermal stratification.

Much of the research literature on wake characteristics in wind farms focuses on fatigue loading effects (Ref. 9) or power extraction and efficiency maximization (Refs. 10–12). Magnusson<sup>13</sup> shows that for the near turbine portion of the wake, momentum transport is carried out by the turbulence generated by the shear profile as well as the turbine itself. Sanderse<sup>14</sup> reviews numerical wake model data on global wind farm aerodynamics and shows that wake recovery of turbines further downstream in the array occurs more quickly than the wake recovery of upstream turbines, and that the increase of turbulence for downstream turbines in fact aids the entrainment of kinetic energy from above the array. A further review of wind farm models by Ref. 15 details the discrepancy between computational models in accounting for wake losses. Overall, however, many questions remain about turbulence and wake characteristics within large turbine arrays. Barthelmie<sup>15</sup> notes that accurate wake recovery quantification is a key issue with wind farm models. Currently, not much is known about characteristics of the flow structures that affect the flow external to turbines and entrain kinetic energy into the array in the vertical direction. A greater understanding of these flow structures is needed, which constitutes the main objective of this study.

In order to identify the terms associated with kinetic energy in the flow, it is useful to begin with the Reynolds averaged momentum equations. At high Reynolds numbers, the Reynolds-Averaged Navier-Stokes boundary layer equation in the streamwise direction read

$$\bar{U} \frac{\partial \bar{U}}{\partial x} + \bar{V} \frac{\partial \bar{U}}{\partial y} + \bar{W} \frac{\partial \bar{U}}{\partial z} = -\frac{1}{\rho} \frac{d\bar{P}}{dx} - \frac{\partial}{\partial x} \overline{u'u'} - \frac{\partial}{\partial y} \overline{u'v'} - \frac{\partial}{\partial z} \overline{u'w'} - \bar{f}_x, \quad (1)$$

where  $u$ ,  $v$ , and  $w$  are the streamwise, vertical, and transverse velocities, respectively, in directions  $x$ ,  $y$ , and  $z$  (here, we use the engineering convention with  $y$  being the vertical direction, and not the atmospheric sciences convention, where  $z$  is usually the vertical direction). An overbar denotes averaging, and capital letters denote time-averaged variables, whereas primes indicate turbulent fluctuations. The quantities with an overbar in Eq. (1) have been averaged in time. Coupled with the assumption of stationarity, the time derivative term has been omitted from the material derivative on the left side of the equation. The Reynolds shear stress or turbulent momentum flux  $\overline{u'v'}$  accounts for recovery of the momentum in the wake in the vertical direction, while spanwise recovery is represented by the Reynolds stress  $\overline{u'w'}$ . The forcing term  $\bar{f}_x$  is the thrust effect of the wind turbine. It acts only in the region where the wind turbines are located. In detail, it is caused by time-dependent pressure and viscous forces acting at the moving blade-air interface and appropriately projected in the streamwise direction. The term  $\bar{f}_x$  is averaged over time to eliminate periodic time-dependence from the rotating blades. In Eq. (1), the viscous term has been neglected due to the consideration that at distances sufficiently far from a surface, the viscous stresses have negligible effect on the mean velocity. In wind farms, Coriolis force terms and buoyancy terms should also be included. Here, they are not included as they are absent in the wind tunnel data to be analyzed in this work. Conclusions reached will be relevant for neutrally buoyant flow, neglecting the Ekman layer turning that is due to Coriolis effects. As discussed in Refs. 3 and 4, these affect mainly the “outer parts” of the flow above the wind farm and the region of interest here, immediately above the wind turbines.

Multiplying the above equation by the mean streamwise velocity and rearranging terms yields a transport equation for the streamwise part of the kinetic energy,  $\overline{U^2}/2$ . The terms involving Reynolds stresses can be decomposed into turbulence production and kinetic energy transport terms, such as for instance,

$$-\overline{U} \frac{\partial}{\partial y} \overline{u'v'} = \overline{u'v'} \frac{\partial \overline{U}}{\partial y} - \frac{\partial}{\partial y} (\overline{U} \overline{u'v'}). \quad (2)$$

The terms  $\overline{u'v'} \frac{\partial \overline{U}}{\partial y}$  and  $-\frac{\partial}{\partial y} (\overline{U} \overline{u'v'})$  are expected to be dominant along the wake center plane, on which  $\frac{\partial \overline{U}}{\partial z}$  and  $\overline{u'w'}$  are negligible due to symmetry (except for contributions from wake angular momentum). The first of these terms,  $\overline{u'v'} \frac{\partial \overline{U}}{\partial y}$ , contributes to loss of mean kinetic energy due to production of turbulent kinetic energy. The second term,  $-\frac{\partial}{\partial y} (\overline{U} \overline{u'v'})$ , represents gradient of flux of kinetic energy in the vertical direction. Using additional averaging over horizontal planes, in Ref. 4, it was shown that the vertical entrainment by turbulence was the most dominant means of entraining kinetic energy into the domain where the wind turbines are located. Additional contributions due to the mean flow spatial inhomogeneities were found to be small. Therefore, in this paper, we focus attention on the flux of kinetic energy defined as

$$F(y) = -\overline{U}(y) \overline{u'v'}(y), \quad (3)$$

whose vertical gradient determines the development of kinetic energy in the flow. The flux  $F(y)$  is also responsible for recovery of kinetic energy in the wake.

The objective of this paper is to analyze turbulent structures at selected locations in the wake centerline plane, specifically quantifying their impact on the vertical kinetic energy flux  $F(y)$ , using techniques of conditional averaging and spectral analysis. In Sec. II of this paper, the statistical tools used for data analysis are briefly reviewed and explained. In Sec. III, we describe the experiments from which the data to be analyzed have been obtained and show some reference data. Results are presented in Sec. IV, and a discussion of the results and conclusions are presented in Sec. V.

## II. ANALYSIS METHODOLOGY

In this section, we describe how the flux term to be studied in this paper,  $F(y) = -\overline{U} \overline{u'v'}$ , is to be further decomposed and analyzed. Specifically, we consider conditional averaging into various velocity fluctuation quadrants as well as a spectral decomposition in order to determine dominant length-scales.

### A. Conditional averaging

Conditional statistical analysis has a long history in the study of turbulent boundary layer flows. The quadrant analysis method delineated by Refs. 17 and 18 for analysis of dominant contributions to the Reynolds shear stress consists of separating the flow into four types of events. Flow events will occupy one of the four quadrants shown in Figure 1. The quadrants are defined depending on the four possible combinations of sign of the instantaneous value of the fluctuating streamwise and wall-normal velocity components. Consistent with the fact that the Reynolds stress ( $-\overline{u'v'}$ ) is positive (i.e., the streamwise and wall-normal velocity fluctuations are typically anti-correlated), flow events are predominantly located in quadrants 2 and 4, known, respectively, as ejections and sweeps. Ejections represent turbulent bursts upward at velocities slower than the mean, as indicated by a negative value of the streamwise fluctuating velocity and a positive normal fluctuating velocity. Conversely, sweeps represent turbulent bursts in the positive streamwise direction and downward, as indicated by the signs of  $u' > 0$  and  $v' < 0$  in quadrant 4.

Quadrant analysis has been employed in various prior studies, such as for studying the generation of coherent structures (Refs. 19 and 20), to study turbulent boundary layers over rough and smooth walls (Ref. 24), for atmospheric boundary layers (Refs. 25 and 26), and also to characterize the wake behind a cylinder (Refs. 21 and 22). Quadrant analysis has also been applied to studying structure of thermal fields.<sup>27,28</sup> Roussinova *et al.* (Ref. 29) performed quadrant analysis in conjunction with proper orthogonal decomposition to track momentum transport and the development of hairpin vortices at varying energy levels in open-channel flows.

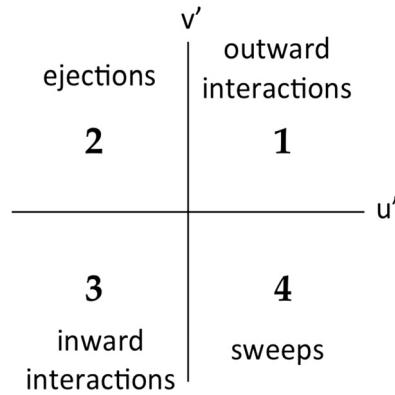


FIG. 1. Diagram showing four quadrants and their nomenclature used in quadrant analysis of turbulent shear flows.  $u'$  is the streamwise velocity fluctuation (deviation from local mean), while  $v'$  is the vertical velocity fluctuation (positive is the normal direction away from the surface).

Conditional averaging and quadrant analysis has also found applications in the analysis of turbulent flows over plant canopies (e.g., Refs. 19, 30–33). Yue *et al.* and Zhu *et al.*<sup>34,37</sup> used quadrant event decomposition to perform a comparative analysis of large eddy simulation (LES) and wind tunnel experiments, respectively, of turbulent flow over a mature cornfield. Both studies found sweeps (quadrant 4 events) and ejections (quadrant 2 events) to play a dominant role for the turbulent kinetic energy evolution inside the canopy, with sweeps being a more significant contributor. Similar results were found in the turbulent canopy over a wheat field (Ref. 38). Katul *et al.*<sup>26</sup> found that sweeps are the dominant coherent structures within dense vegetative canopies, while ejections dominate in sparse canopies. A key ingredient of canopy sublayers is that drag forces affect the flow over a distributed region in the vertical direction. In this regard, since wind turbines are accompanied by drag forces in the streamwise direction, wind turbine arrays could be considered as a canopy sublayer.<sup>16</sup>

A more in-depth characterization of the various quadrants can be achieved by introducing dependence upon the magnitude of the fluctuations. Specifically, the *quadrant-hole* analysis involves a conditional averaging denoted by  $\langle \dots \rangle_{i,H}$  and is used to determine the contributions to particular flow variables from each quadrant depending on the relative magnitudes of  $u'$  and  $v'$ . Specifically, the quadrant hole conditional averaged Reynolds shear stress is defined (Refs. 23 and 24) according to

$$-\langle u'v' \rangle_{i,H}(y) = -\lim_{T \rightarrow \infty} \frac{1}{T} \int_0^T u'(t,y)v'(t,y)I_{i,H}[u'(t,y)v'(t,y)] dt, \quad (4)$$

where  $i$  is the quadrant (i.e.,  $i = 1, 2, 3$ , or  $4$ ),  $T$  is the averaging time period, and  $H$  is the “hole size,” used as an indicator of the magnitudes retained. The function  $I_{i,H}$  is a step function that takes a unit value when  $u'$  and  $v'$  are in quadrant  $i$ , and the absolute value of their product lies above a threshold,  $H$ ,

$$I_{i,H}(u'(t,y)v'(t,y)) = \begin{cases} 1, & \text{if } (u', v') \text{ is in quadrant } i \text{ and } |u'v'| \geq H, \\ 0, & \text{otherwise.} \end{cases}$$

Quadrants 2 and 4, known as ejections and sweeps, respectively, both contribute to the Reynolds stress  $-\overline{u'v'} > 0$ .

The conditional averages can be utilized (Raupach<sup>24</sup>) to define the stress fractions

$$S_{i,H}(y) = \frac{\langle u'v' \rangle_{i,H}(y)}{\overline{u'v'}(y)} \quad (5)$$

and the duration fraction

$$D_{i,H}(y) = \frac{1}{T} \int_0^T I_{i,H}[u'(t)v'(t); y] dt, \quad (6)$$

indicating the relative durations of each of the quadrant events. When no threshold is imposed on the magnitude, i.e., when  $H=0$ , all events are considered in the analysis, and

$$\sum_{i=1}^4 S_{i,0}(y) = \sum_{i=1}^4 D_{i,0}(y) = 1. \quad (7)$$

The above conditional averages relate to the contributions of the fluctuations to the momentum fluxes. The associated kinetic energy fluxes can be similarly analyzed by introducing the quadrant turbulent flux of kinetic energy, defined as

$$F_i(y) = -\langle u'v' \rangle_{i,0} \bar{U}(y). \quad (8)$$

With this definition, the additivity properties of the quadrants are maintained. This definition suggests decomposing the velocity fluctuations in terms of their product with  $\sqrt{\bar{U}}$ , i.e., we introduce a plane of  $\sqrt{\bar{U}}u' - \sqrt{\bar{U}}v'$  axes. In this plane, a quadrant hole analysis associated with kinetic energy fluxes can be defined according to

$$J_{i,H_F}(u'v') = \begin{cases} 1, & \text{if } (u', v') \text{ is in quadrant } i \text{ and } \bar{U}|u'v'| \geq H_F; \\ 0, & \text{otherwise.} \end{cases}$$

where  $H_F$  is the hole-size relevant to kinetic energy. The kinetic energy flux fraction can then be defined as

$$F_{i,H_F}(y) = \frac{\bar{U}(y) \langle u'v' \rangle_{i,H_F}(y)}{\bar{U}(y) \overline{u'v'}(y)}, \quad (9)$$

such that at a threshold of  $H_F = 0$ , the values of stress fraction and flux fraction are identical.

To illustrate the concept of quadrant-hole analysis, Figures 2(a) and 2(b) show the  $u' - v'$  and  $\sqrt{\bar{U}}u' - \sqrt{\bar{U}}v'$  planes, respectively, with contours of constant  $H$  or  $H_F$  in each quadrant. For a given value of  $H$  or  $H_F$ , those contributors to the downward flux that lie outside the constant contour (in the shaded regions) are included in the averaging. Those inside the constant contour (the white regions) are considered to be within the “hole” and are ignored in the fractional calculation. At a threshold of  $H=0$ , the contours shrink to a point at the origin, thus allowing all contributions to be retained. As the threshold increases, the number of terms lying above the contours decreases, and fewer fluctuations are retained in the evaluation of the conditional averages.

The analysis will also consider contributions of each quadrant to the viscous dissipation rate  $\epsilon$ . The dissipation rate is formally defined<sup>39</sup> in terms of gradients of all velocity components in all three spatial directions. For point-measurements, a commonly used approximation, assuming small-scale isotropy, is given by

$$\epsilon = 15\nu \overline{\left( \frac{\partial u'}{\partial x} \right)^2}, \quad (10)$$

where  $\nu$  is the kinematic viscosity of the fluid. Additionally, Taylor’s hypothesis can be invoked to approximate the spatial derivative using time derivatives. Taylor’s hypothesis assumes that a time-series data can be interpreted as a spatial streamwise cut through a frozen flow field. As a result, derivatives may be evaluated according to



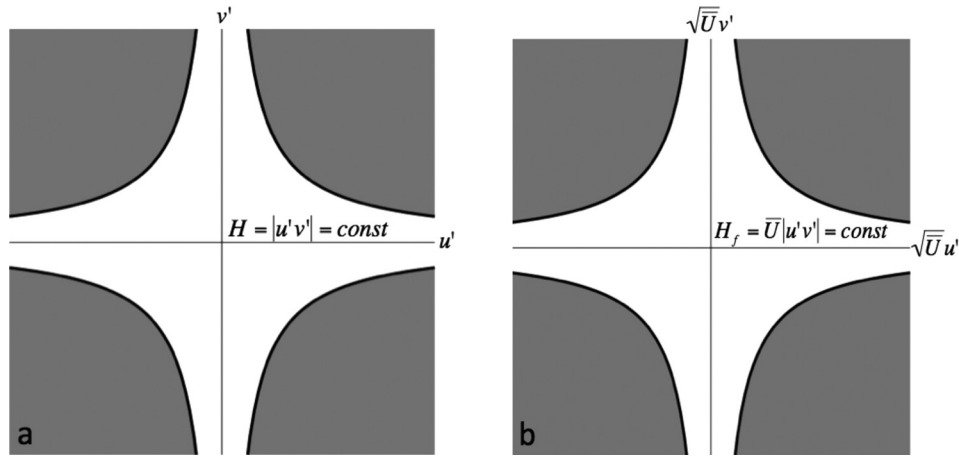


FIG. 2. Schematic diagram of conditional averaging domains used in “quadrant-hole” analysis of turbulent shear flows. (a) The traditional approach in which the threshold is identified at a constant  $H = |u'v'|$  level. (b) The “kinetic energy flux” quadrant hole analysis used here, with axes  $\sqrt{U}u'$  and  $\sqrt{U}v'$  so that lines of constant  $H_F$  correspond to thresholds on  $H_F = \bar{U}|u'v'|$ .

$$\frac{\partial u}{\partial x} \approx -\frac{1}{\bar{U}} \frac{\partial u}{\partial t}. \quad (11)$$

The approximation is valid in low turbulence regimes. The turbulence intensity,  $Tu$ , is defined as

$$Tu = \frac{\sqrt{\overline{(u')^2}}}{\bar{U}}, \quad (12)$$

where the prime signifies velocity fluctuations. In our experiment, the turbulence intensity is between 15% and 20%. A turbulence intensity at this level is considered borderline for applicability of Taylor’s hypothesis. However, the trends observed in this study are not expected to be significantly affected by the application of this approximation. Thus, the corresponding dissipation fraction in each quadrant,  $S_i^\epsilon(y)$ , can be defined according to

$$S_i^\epsilon(y) = \frac{\langle (\partial u' / \partial x)^2 \rangle_{i,0}(y)}{(\partial u' / \partial x)^2(y)}. \quad (13)$$

Equation (10) assumes that the small-scales of turbulence that determine the rate of dissipation are isotropic in an average sense. Equation (13) further assumes that isotropy also holds within each quadrant. The large-scale structure of the flow (as determined by  $u'$  and  $v'$  falling into particular quadrants) is often assumed to not affect the statistics and geometric structure of small scales in turbulence, and so Eq. (13) would be justified based on this usual assumption. However, as will be seen in the actual measurements, some influence of  $u'$  and  $v'$  on the magnitude of dissipation is present. The approximate nature of Eq. (13) must therefore be kept in mind when interpreting the results.

## B. Spectral analysis

Spectral analysis has been used in numerous studies to determine the contribution from specific length or time scales to total variances and fluxes. The most energetic scales of turbulent flows will correspond to peaks in the relevant spectra. In studies of wind turbine flows, the technique is largely used in failure analysis and to understand turbine and array power output. Few studies have employed spectral analysis to determine relevant turbulent length-scales in wind

turbine wakes. Morfiadakis<sup>40</sup> obtained power spectra of flow within a complex-terrain wind farm and found limitations to the applicability of the von Kármán spectrum to describe the turbulence structure due to turbine wake effects. Crespo and Hernández<sup>41</sup> employed spectral analysis to study diffusion of the velocity defect created by the near wake drag of single wind turbines.

Here, spectral analysis is employed to determine which length-scales in the flow contribute most significantly to the vertical flux of momentum (Reynolds stresses) as well as of flux of kinetic energy. Spectra and co-spectra are evaluated based on hot-wire signals decomposed using fast Fourier transform (FFT) algorithm. Specifically, the cospectrum,  $\Phi_{-uv}(k; y)$ , is defined according to

$$\Phi_{-uv}(k; y) = -\langle \mathcal{F}_u(k; y) \mathcal{F}_v^*(k; y) \rangle, \quad (14)$$

where  $k$  is the wavenumber,  $\mathcal{F}_u$  is the Fourier transform of the streamwise velocity, and  $\mathcal{F}_v^*$  is the complex conjugate of the wall-normal velocity's Fourier Transform. The original data taken in the wind tunnel is a time-series, whose Fourier transform is given as function of frequency.

To present the spectra in terms of wavenumber, again Taylor's frozen flow hypothesis is invoked. Therefore, the relationship between streamwise wavenumber  $k$  and frequency  $f$  is given by  $k \equiv 2\pi/(U/f)$ . The integral of the cospectrum  $\Phi_{-uv}(k; y)$  over wavenumber  $k$  yields the Reynolds shear stress, as

$$-\overline{u'v'}(y) = \int \Phi_{-uv}(k; y) dk. \quad (15)$$

Typically, spectra and cospectra in turbulence display power-law behavior. As a result, the premultiplied (Ref. 42) spectrum  $k\Phi_{-uv}(k; y)$  can be used to describe the contributions of various length-scales ( $\sim 1/k$ ) to the total shear stress. Similarly, if one is interested in contributions of various length-scales to the vertical flux of kinetic energy, one may introduce the premultiplied cospectrum that also includes the mean velocity at any given height as follows:

$$E_{-uv}^F(k; y) = k\Phi_{-uv}(k; y)\overline{U}(y). \quad (16)$$

Integration over  $k$  (instead of premultiplication by  $k$ ) yields the vertical flux of kinetic energy.

In order to correlate the streamwise and wall-normal flow characteristics at each point as a function of the spatial scales, the spectral coherence is defined as in Ref. 43

$$coh(k; y) = \sqrt{\frac{Q(k; y)^2 + Co(k; y)^2}{\Phi_{uu}(k; y)\Phi_{vv}(k; y)}}, \quad (17)$$

where  $Q(k; y)$  is the quadrature spectrum,  $Co(k; y)$  is the coherence spectrum, and  $\Phi_{uu}(k; y)$  and  $\Phi_{vv}(k; y)$  are the longitudinal spectra of streamwise and wall-normal velocity components. As noted in Ref. 43, there is a gap in our understanding of coherence in the non-equilibrium turbulence of wind turbine wakes. While most prior use of spectral coherence has been to determine the coherence between a single velocity direction at two locations, in this study, we consider the coherence between the streamwise and wall-normal velocities at a single point, in order to analyze the turbulent coherence at various scales of the flow contributing to the shear stress. The coherence spectrum of the shear stress and of the vertical kinetic energy spectra are equivalent, since the multiplication by mean velocity cancels in the numerator and denominator of Eq. (17).

### III. EXPERIMENTAL SETUP

The experiment was conducted in the Corrsin Wind Tunnel (Refs. 44 and 45) at the Johns Hopkins University. It is a return-type wind tunnel with two contractions. The test section is 10m long, 0.9m high, and 1.2m wide. Strakes and an active grid at the inlet are employed to generate a mean shear profile and significant free stream turbulence. Inside this test section, a



$3 \times 3$  array of lightly loaded model wind turbines of rotor diameter  $D = 0.12$  m and tower height  $H = 0.12$  m were placed within a turbulent boundary layer over a rough surface. The freestream mean velocity was 9.4 m/s. The turbines were spaced  $3D$  in the transverse direction and the spacing between rows was  $7D$  in the streamwise direction. Further details about the turbines, their position, and the experimental setup are provided in Ref. 4. Because the characteristic velocities and fluid viscosity are similar in the wind tunnel to those in the field, the Reynolds number ratio is the same as the ratio of typical length-scales, i.e., about a factor of 830. Based on rotor diameter and hub-height mean velocity at the data-location used here, the wind tunnel Reynolds number is about  $4.5 \times 10^4$ , whereas in the field, Reynolds numbers of  $4 \times 10^7$  can be expected. Therefore, except to the flow details very close to the turbine blades, both the wind tunnel and the field-scale Reynolds numbers are quite large. This is used to invoke asymptotic invariance on Reynolds number, for the characteristics of the large-scale structure of turbulence. In fact, recently, it was shown in a detailed and extensive experimental wind tunnel study<sup>36</sup> that, except in the near wake area ( $x/D < 3$ ), mean velocity and turbulence statistics in wind turbine wakes demonstrate Reynolds number independence for  $Re > 9 \times 10^4$ . For  $Re > 4.5 \times 10^4$ , mean velocities were indistinguishable from those at much higher  $Re$  (Fig. 4 of Ref. 36), and turbulence standard deviation differed only by about 3% from its values at very high Reynolds numbers (Fig. 6 of Ref. 36). While the limitations of the Reynolds number mismatch have to be kept in mind, we deduce based on the scaling arguments as well as the results of Ref. 36 that the effects of Reynolds number on the observed statistics of large-scale turbulence can be neglected.

Velocity data were acquired using X-type hotwire anemometry. The X-wire probe was calibrated in the core region of an axisymmetric calibration jet. 15 different jet-exit velocities as well as nine different jaw angles were used for the calibration within the speeds. The probe alignment was kept fixed during the variation in velocity while variations in jaw call for a fixed velocity during the calibration. The velocity calibration of the hot wires was repeated at four different fixed temperatures, which took into account the thermal variation while performing the experiment. The hot-wire anemometer produced stable signals during the entirety of the experiment.

Measurements were taken for 100 s at each of a set of sampling locations, covering one streamwise and one transverse plane, which intersect to form a cross, 0.6 m behind the middle turbine of the last row downstream. Figure 3 presents a schematic of the experimental setup. Data were acquired at a sampling frequency of 40 kHz. Measurements for streamwise and wall-normal velocities were taken first, then the hotwire was rotated to measure the streamwise and transverse velocities. The transverse plane was used to measure streamwise, wall-normal, and transverse velocities at 9 locations spaced  $1/6D$  apart, at the wake centerline. The streamwise plane was used to measure velocities at  $1D$  increments. In both planes, 21 vertical locations were considered at 0.01 m increments, beginning 0.005 m from the bottom surface. The

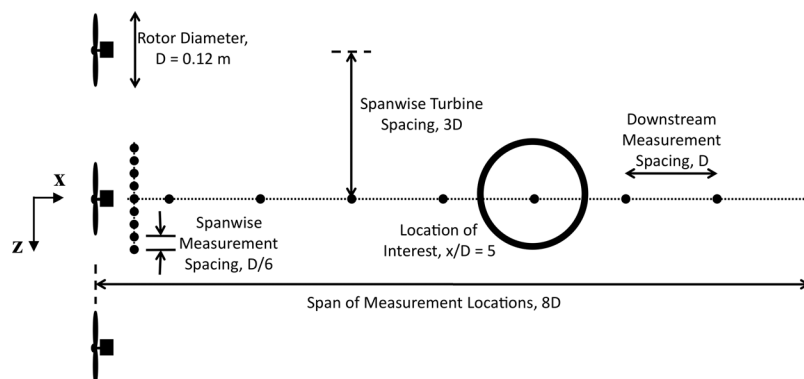


FIG. 3. Schematic of streamwise and transverse measurement locations behind the middle turbine of the last row in model wind farm. Each filled circle indicates a location where 21 vertical measurements (along  $y$ -direction) were made. The circle indicates the measurement location at  $x/D = 5$ , the profile location at which most of the present analysis is performed.

streamwise, wall-normal, and transverse directions are denoted as the  $x$ ,  $y$ , and  $z$  Cartesian coordinates.

Figures 4–6 show profiles of mean streamwise velocity, streamwise velocity variance, and Reynolds shear stress at various streamwise locations in the wake centerline. All three figures were normalized by either the freestream velocity,  $u_o$ , of 9.4 m/s in Figure 4 or by the square of the freestream velocity,  $u_o^2$ , in Figures 5 and 6. The average streamwise velocity shows a significant reduction in the near wake (at the nacelle of the turbine),  $x/D = 1$ ,  $y/D = 1$ . The velocity steadily recovers as the flow moves downstream, with diminishing changes as a function of streamwise distance clearly visible in the similarity of profiles at  $x/D = 7$  and  $x/D = 8$ . The measurement location at  $x/D = 5$  is the first profile that shows vertical monotonicity, defined by a uniformly increasing velocity at each subsequent vertical location. This contrasts, for instance, with the profile at  $x/D = 1$ , where the velocity decreases from the bottom of the wake to the middle. In this paper, the focus will be on the profile at location  $x/D = 5$ , since it is more representative of the intermediate and far-wake profile behavior.

The streamwise velocity variance in the near wake shows a characteristic “double hump” (cf. with velocity profiles in Ref. 13). The effects of the hub create largely reduced variances near  $y/D = 1.1$ . The variances are also reduced downstream, as turbulence intensity decreases with wake recovery. By  $x/D = 8$ , the variance in  $y$ -direction becomes relatively small over the entire profile. Similarly, the Reynolds shear stress achieves the steepest gradient in the near wake, with the lowest gradient occurring at  $x/D = 8$ . At nacelle height,  $y/D = 1.1$ , the Reynolds shear stress stays approximately constant in the downstream direction. All shear stress profiles display an inflection point at this approximate height. Because the profile shown is of  $-u'v'$  (including the minus sign), positive values represent net downward momentum flux, while negative values, where they occur, represent a net upward flux. In the near wake,  $x/D = 1$ –4, the lower wake area (as indicated by the bottom horizontal line) displays upward momentum flux with the wake replenishing momentum from the flow below. At  $x/D = 5$  and beyond, all momentum flux is downward. As mentioned above, the following analysis focuses on vertical profile data of the downstream distance  $x/D = 5$ .

This location represents a downstream point typical of the intermediate wake region in which there is strong wake-boundary layer interaction. Figure 7 shows the profile of the Reynolds shear stress,  $-\langle u'v' \rangle$ , and the correlation coefficient profile,  $\rho_{-\langle u'v' \rangle}$ . Horizontal lines at

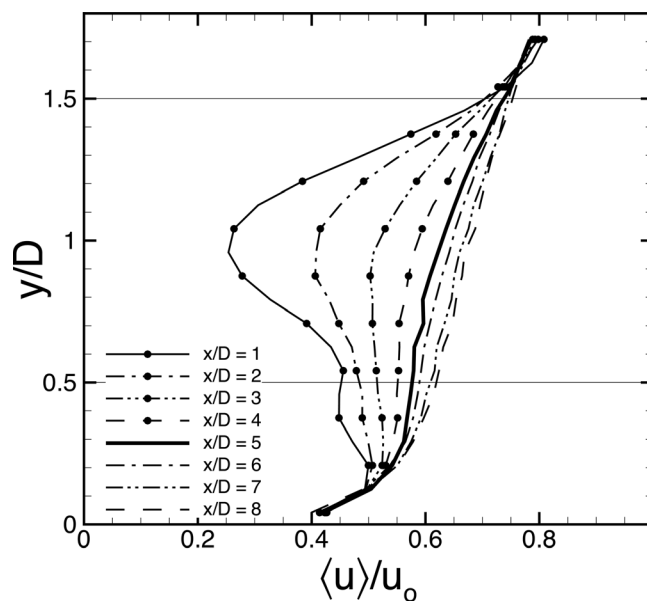


FIG. 4. Profiles of the average streamwise velocities at eight streamwise locations in the turbine wake. Horizontal lines indicate the rotor wake area at  $y/D = 0.5$  and  $y/D = 1.5$  ( $D = 0.12$  m).

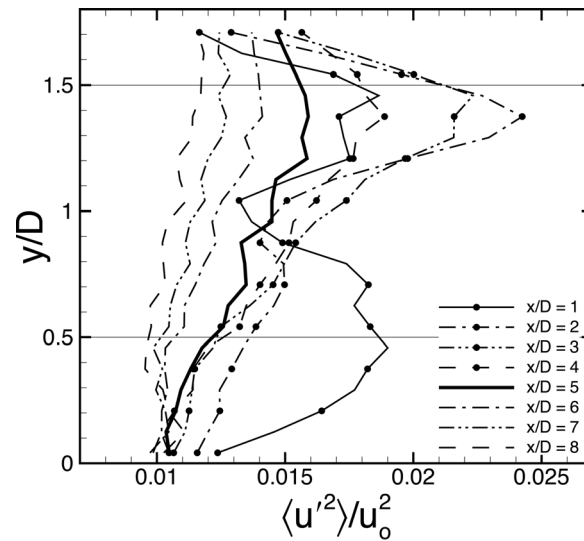


FIG. 5. Profiles of stream-wise velocity variance at eight locations in the turbine wake. Horizontal lines indicate the rotor wake area.

$y/D = 1.5$  and  $0.5$  indicate the top and bottom of the rotor area, respectively. Both profiles show an order of magnitude drop in their values from the top to bottom of the rotor area. The Reynolds shear stress is highest at the top of the rotor area,  $0.375 \text{ (m/s)}^2$  and lowest at the bottom of the rotor wake area,  $0.03 \text{ (m/s)}^2$ . The correlation coefficient exhibits a similar profile shape, with a value of  $0.4$  at the top of the wake and a value of  $0.05$  at the bottom of the rotor wake area.

Section IV presents results specifically geared to quantifying the contributions of various flow events and length-scales to the vertical flux of kinetic energy.

#### IV. RESULTS

Figures 8 and 9 show, respectively, the quadrant analysis of the Reynolds stress  $-\langle u'v' \rangle$  and kinetic energy flux. As a validation of the quadrant analysis technique and calculations,

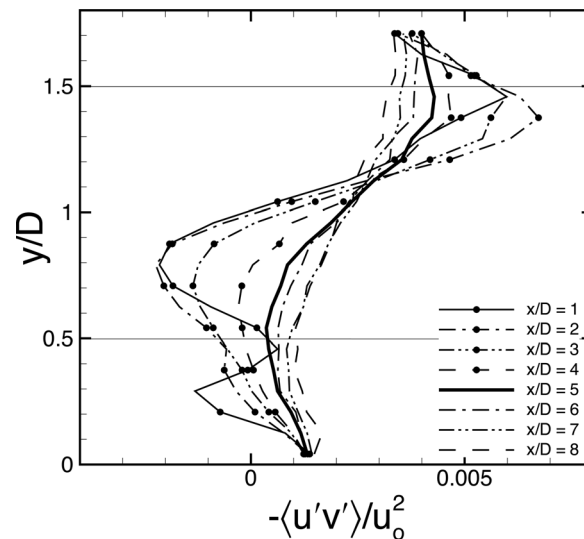


FIG. 6. Profiles of the Reynolds shear stress at eight streamwise locations in the turbine wake. Horizontal lines indicate the rotor wake area.

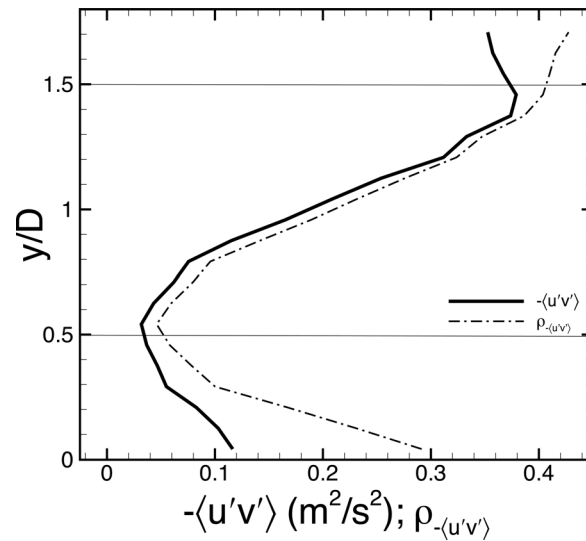


FIG. 7. Profiles of the Reynolds stress (solid line) and  $u' - v'$  correlation coefficient (dot-dashed line) at the selected  $x/D = 5$  downstream location used for additional analysis. Horizontal lines indicate the rotor wake area.

the sum of the quadrant stress profiles recovers the profile of the Reynolds stress shown in Figure 7. Likewise, the sum of all quadrants in Figure 9, the total vertical flux of kinetic energy, is shown. A positive value denotes a contribution to downward flux, while a negative value denotes a vertically upward flux contribution. Visualizing a control volume spanning from the bottom to the top of the wind turbine region, the difference in fluxes between the top and bottom of the rotor wake indicates the net contribution to power available to turbines downstream (see Ref. 4). The downward flux is  $2.5 \text{ m}^3/\text{s}^3$  at the top of the wake and  $0.2 \text{ m}^3/\text{s}^3$  at the bottom of the wake. With an air density of  $1.20 \text{ kg}/\text{m}^3$ , a net flux of  $2.8 \text{ W}/\text{m}^2$  is thus entrained into the wake area at that position. Using horizontally averaged data in the same flow (using 3D meanflow distributions measured using PIV), Cal *et al.* obtained a net entrainment rate of  $1.8 \text{ W}/\text{m}^2$ . The smaller value obtained in that study is attributable to the averaging over all areas, including areas between the wakes and not just at the wake centerline. This

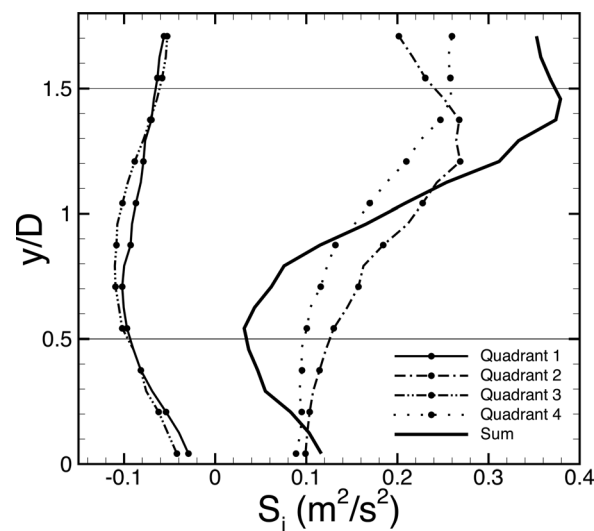


FIG. 8. Profiles of contributions,  $S_i$ , from each quadrant to the total Reynolds stress profile. The hole-size threshold,  $H$ , here is zero and all realizations of the stress  $-\overline{u'v'}$  are included. The sum of all quadrants (solid line,  $S = -\overline{u'v'} = \sum S_i$ ) is also shown. Summing the contributions of the Reynolds stress profiles from all 4 quadrants recovers the profile depicted in Figure 7.

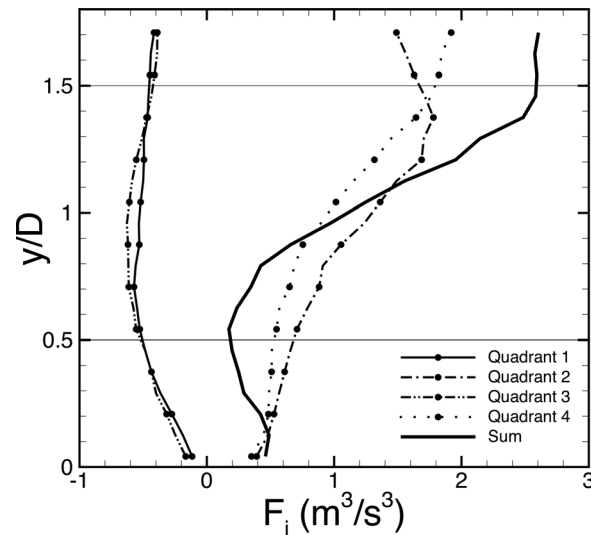


FIG. 9. Profiles of contributions,  $F_i$ , from each quadrant to the flux of turbulent kinetic energy, again with a hole-size threshold,  $H$ , of zero. The sum of all quadrants (solid line,  $F = -\overline{U} \overline{u'v'} = \sum F_i$ ) is also shown. Each profile above is the product of the mean streamwise velocity,  $\overline{U}$ , and the respective profile of  $S_i$  shown in Figure 8. The net power entrained into the wake at the measurement location is the difference between  $F$  at the top and bottom of the rotor wake area (at  $y/D \approx 1.5$  and  $y/D \approx 0.5$  shown as horizontal lines).

effect is reflected by the data here and results in a net positive entrainment of kinetic energy downward from the flow above the turbine canopy into the wake. Thus, Figures 8 and 9 imply that maximizing the vertical entrainment of kinetic energy into the wake maximizes the power available to subsequent turbines.

As can be seen clearly in the profiles shown in Fig. 9, sweeps and ejections are both similar contributors to the downward turbulent kinetic energy flux. The ejection flow structures (from quadrant 2) make a slightly greater contribution over most of the profile in comparison to the sweeps (quadrant 4). Across the wake, there are significantly larger changes in sweep and ejection contributions as compared to outward and inward interaction contributions (quadrants 1 and 3, respectively). The value of sweep and ejection type fluxes of kinetic energy decrease by about two-thirds, whereas the outward and inward interaction contributions do not change much over the wake area. In the above wake area, sweeps are a main contributor to downward flux.

It may be useful to clarify the observation that ejection events can contribute to downward flux of kinetic energy, since at first sight it may appear to be counter-intuitive. Recall that the flux has been defined by multiplying the momentum fluxes by the overall mean velocity ( $\overline{U}$ ) rather than the actual velocity ( $\overline{U} + u'$ ). Because of this, even ejection events are associated with downward flux of kinetic energy in the mean flow (but not in the turbulence).

In Figures 10–12, quadrant fractions of stress, kinetic energy, and duration are shown for various hole sizes and four vertical locations: close to the bottom surface ( $y/D = 0.042$ ), the bottom wake area ( $y/D = 0.46$ ), the top wake area ( $y/D = 1.46$ ), and the above wake flow ( $y/D = 1.71$ ). The stress fraction is much greater at the bottom of the wake than at any other location due to the typically low value of the Reynolds stress in this area. With the exception of the bottom wake location, the stress fractions in quadrants 1 and 3 are negligible contributors to the total Reynolds stress. Sweeps (quadrant 4) and ejections (quadrant 2) demonstrate a more significant contribution for all wake locations shown. Sweeps are somewhat more persistent for larger hole sizes, which indicates slightly larger magnitudes of the sweep values in their stress contribution. The fractions of kinetic energy fluxes are plotted for hole sizes ranging from 0 to  $50 \text{ (m/s)}^3$ . In Ref. 27, it is explained that sweeps are dominant in dense canopies while ejections are dominant in sparse canopies. Figure 10 shows that these two types of events are roughly equal in their contributions to total Reynolds stress, and therefore we cannot use the observations to catalogue the wind turbine array boundary layer as either dense canopy or a sparse one.

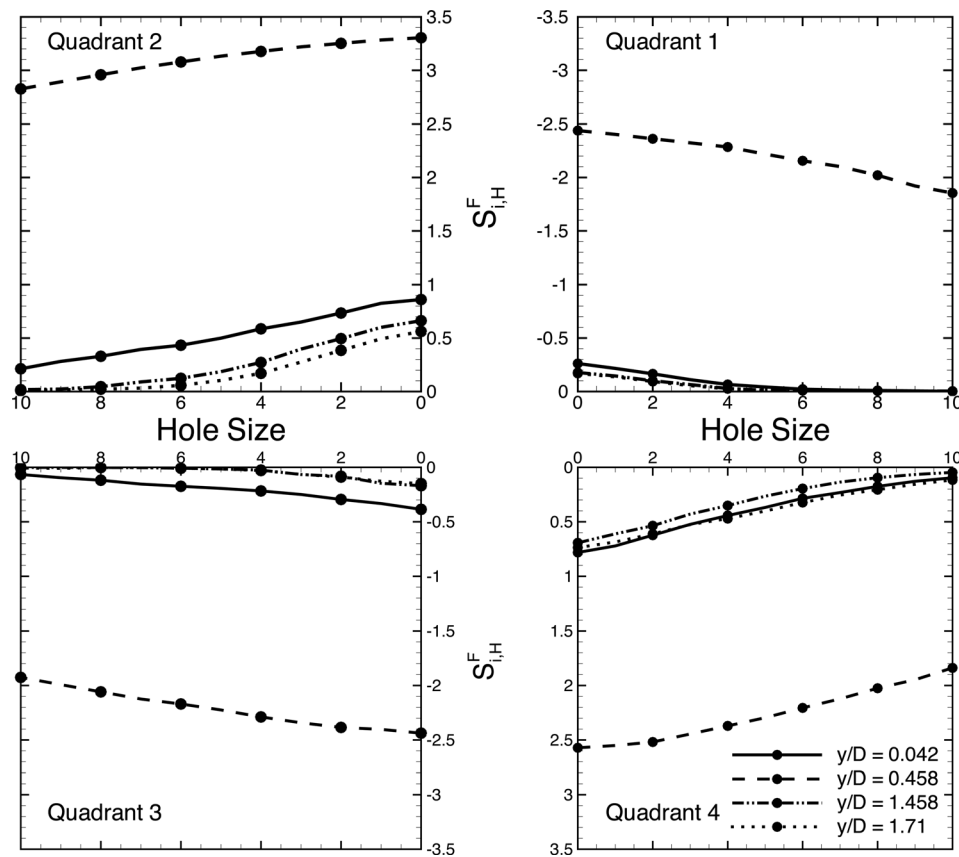


FIG. 10. Quadrant stress fractions,  $S_{i,H}^F$ , at four vertical locations: proximate to the wall ( $y/D = 0.042$ , solid line and circles), bottom of the wake ( $y/D = 0.458$ , dashed line and circles), top of the wake ( $y/D = 1.458$ , dot-dashed line and circles), and the above wake ( $y/D = 1.71$ , dotted line and circles). Hole size  $H$  is given in  $(\text{m/s})^2$ .

The salient features (beyond the persistence of trends at greater hole sizes) in the flux quadrant fractions are the relative differences between the four vertical locations. The bottom wake location  $y/D = 0.46$  shows a greater representation in all quadrants, which is skewed due to the low magnitude of shear stress at that location. The net stress is near zero because contributions from the four quadrants nearly cancel one another out. At the location above the wake ( $y/D = 1.71$ ), it is observed that sweeps are a significantly greater fraction of downward momentum flux than ejection events. Moreover, the contribution due to large sweep events (occurring at large hole sizes) is much greater than the contribution due to large ejection events. The same trends can be noticed in the upper wake flow,  $y/D = 1.46$ , though the difference between fractions of contributions and ejections is less pronounced. At the near wall location, contributions to downward momentum flux decrease rapidly with increasing hole size. The phenomenon is opposite regarding ejections, quadrant 2. The upper and above wake flows exhibit fewer extreme ejection events than does the near wall location. Quadrant 3 exhibits an unusually large fraction at all hole sizes for the near wall location.

The quadrant duration fraction provides complementary information about the stress fractions and enables one to distinguish whether the flow structures are small in magnitude but long-lived or short and very intense. Such analysis has been insightful in characterizing the stresses within plant canopies, as in the work of Ref. 34, who found that at the top of a corn canopy, half of the stress was due to events occurring only 10% of the time. Figure 12 demonstrates, again with the exception of the bottom wake area ( $y/D = 0.46$ ), that outward and inward interactions are of small duration, becoming negligible (less than 3%) at  $H \geq 4 (\text{m/s})^2$ . Sweeps and ejections show significant event length, with the duration of sweeps being larger than the duration of ejections at the bottom wake location. At the top wake location, the relative



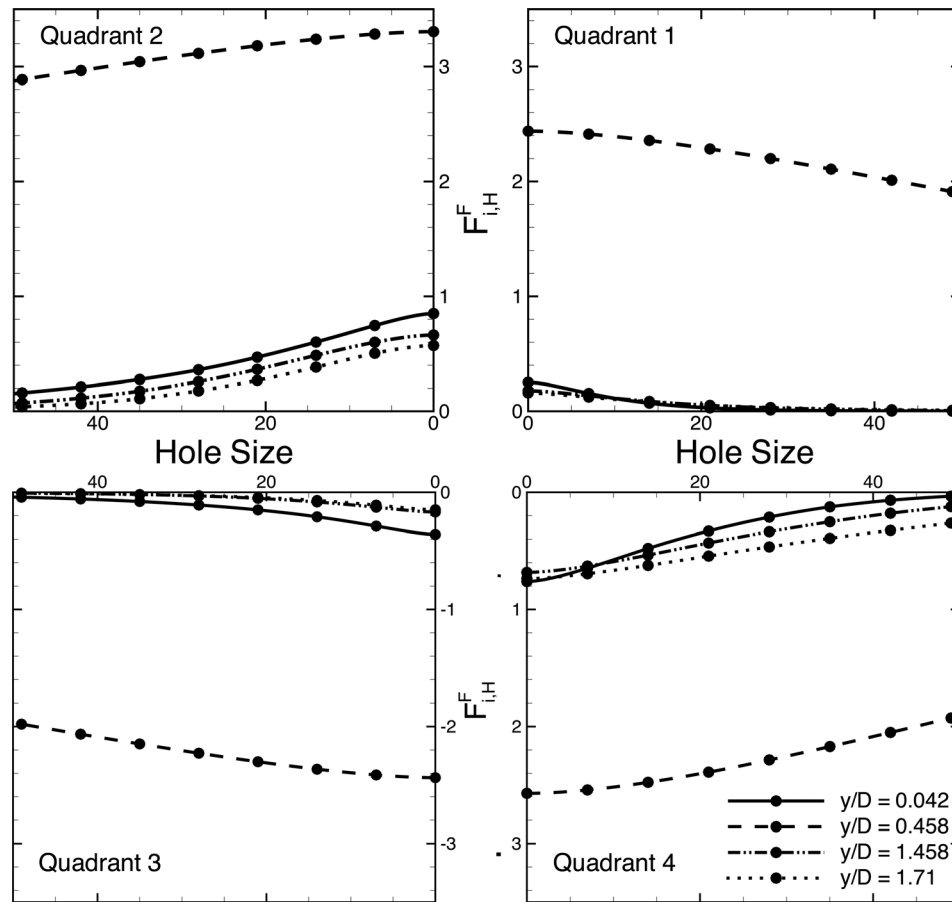


FIG. 11. Quadrant kinetic energy flux fractions,  $F_{i,H}^F$ , at four vertical locations: proximate to the wall ( $y/D = 0.042$ ), bottom of the wake ( $y/D = 0.458$ ), top of the wake ( $y/D = 1.458$ ), and above wake ( $y/D = 1.71$ ). In this figure, the flux hole size  $H_F$  is given in  $(\text{m/s})^3$ .

durations of sweep and ejection events are similar, though sweeps show a slightly greater total duration of high intensity events ( $H \geq 10 (\text{m/s})^2$ ).

Figure 13 shows profiles of the quadrant contribution to viscous dissipation. Each profile indicates  $S_i^e(y)$ , the fraction of the total viscous dissipation found in a particular quadrant. Unlike the shear stress contributions, all four quadrants contribute positively to total dissipation (since dissipation is positive everywhere by definition). The figure shows ejections and sweeps composing the largest contribution to viscous dissipation in the profile at the top of the rotor wake area, where momentum is entrained from the above-wake flow. Ejections at this location are slightly (17%) larger contributors than sweeps. Flow structures in quadrants 2 and 4 are twice as important to dissipation as the structures in quadrants 1 and 3. As the wall is approached, ejection structures show significantly reduced contributions to the dissipation. At the bottom of the rotor wake area, indicated by the lower horizontal line, ejections have lost about a third of their contribution to viscous dissipation, being on the same order as the inward and outward interactions. The sweep contributions, however, remain fairly unchanged over the entire height. Quadrants 2 and 4 provide almost twice the contributions of quadrants 1 and 3 at the top region, where the most relevant contributions to kinetic energy entrainment into the wind turbine array take place. This implies that small-scale turbulence, which determines the dissipation rate, is strongly affected by the large-scale structure of the flow. In the lower parts of the wake, where the shear stress is smaller, the dissipation appears to be less connected to the large-scale structure of the flow.

More quantitative information about length scales can be obtained using cospectra. To evaluate cospectra from the velocity time series, data segments of 4096 samples were transformed

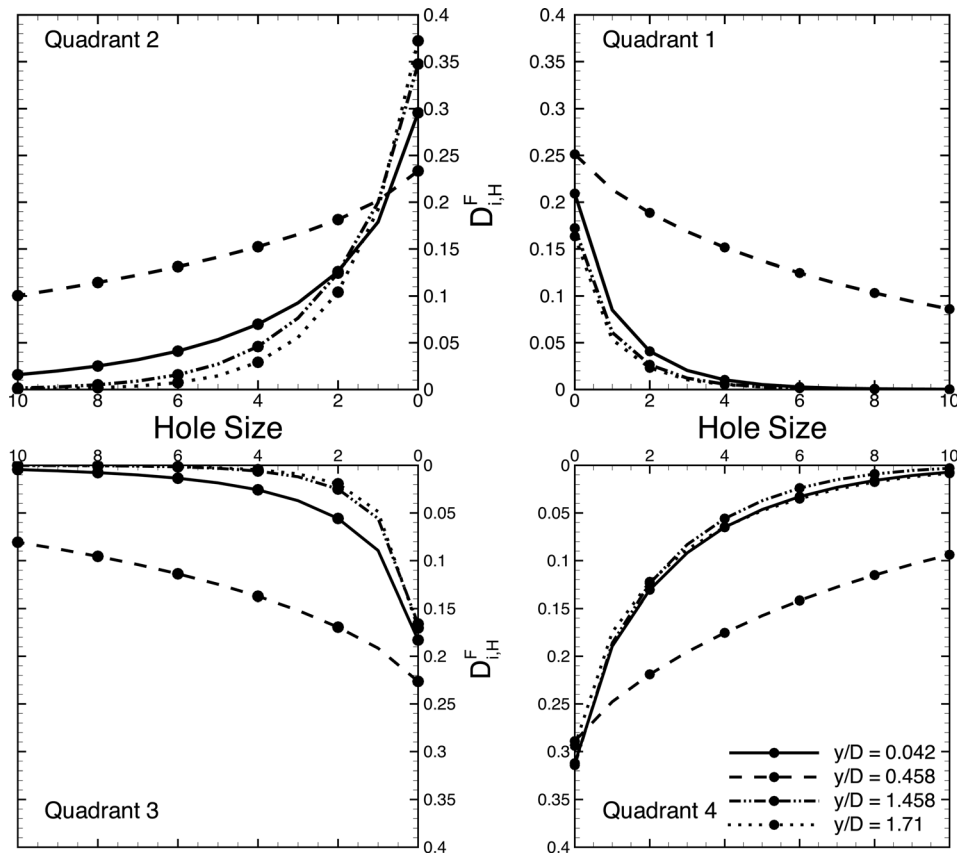


FIG. 12. Quadrant duration fractions,  $D_{i,H}^F$ , at four vertical locations (legend is the same as in Figs. 10 and 11).

using the FFT. Averaging over  $2^6$  segments was performed in order to obtain well-converged cospectra. Figure 14 shows cospectra of the wall normal and streamwise components of velocity at four vertical locations behind the turbine. The cospectra show the characteristic  $-7/3$  slope,<sup>35</sup> with the deviations becoming more noticeable at wavenumbers larger than  $650\text{ m}^{-1}$ , although the general trend still shows good agreement with the expected slope. Differences in

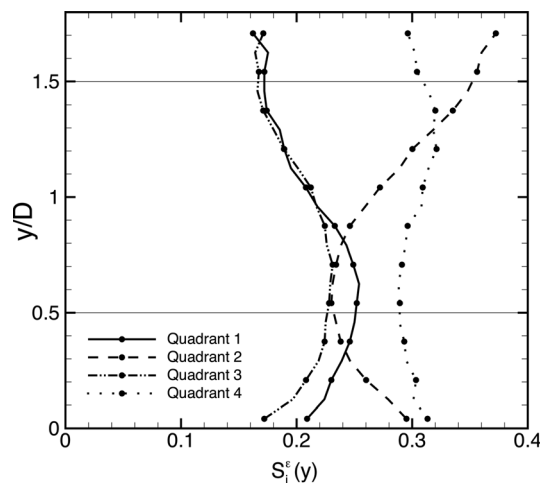


FIG. 13. Profiles of the fractional quadrant contributions to (surrogate) viscous dissipation. Taylor's hypothesis is used to approximate the spatial derivative using measured time derivatives of streamwise velocity.

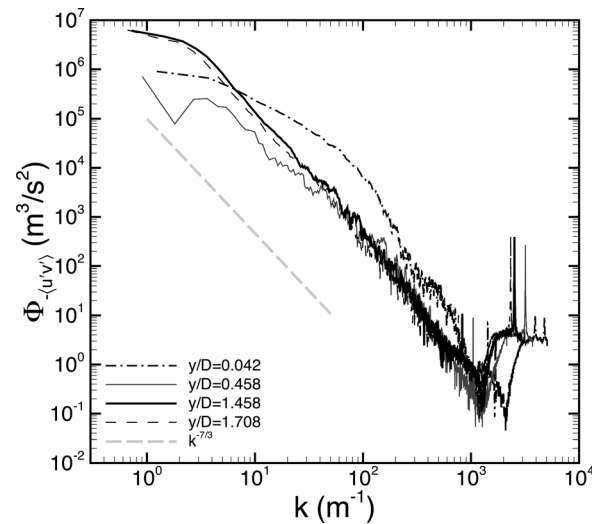


FIG. 14. Cospectra of  $u'$  and  $v'$  fluctuations at vertical locations corresponding to the bottom-most hotwire location ( $y/D = 0.042$ ), the bottom of the turbine wake ( $y/D = 0.458$ ), the top of the turbine wake ( $y/D = 1.458$ ), and the topmost hotwire position ( $y/D = 1.708$ ). The figure omits the highest wavenumber range for clarity. The classic  $\sim k^{-7/3}$  power-law slope line is shown for reference.

wavenumber of the first data point are caused by differences in mean streamwise velocity at each location used when applying Taylor's hypothesis. As can be seen, both the "top of wake area",  $y/D = 1.46$ , and the "above wake area",  $y/D = 1.71$ , show very similar slopes as well as magnitudes. However, the near-wall measurement location at  $y/D = 0.042$  shows significant deviations from the  $-7/3$  scaling, though the magnitude is greater. There, wall effects cause deviations from classical scaling behavior that is more typical of unbounded shear flow. The lower magnitude of the cospectrum at the "bottom wake area" is consistent with the generally low correlation between  $u'$  and  $v'$  at  $y/D = 0.46$ , as seen in Figure 7.

In order to determine the relative contribution to the vertical kinetic energy flux across the entire wake profile, Figure 15 shows a profile of the premultiplied cospectrum of turbulent kinetic energy. As full spectra cannot be shown for all wavenumbers, they are divided into bins

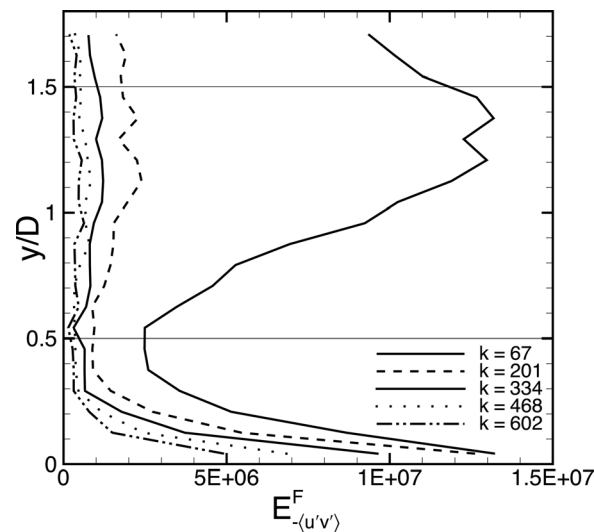


FIG. 15. Profile of the premultiplied cospectral density contributions to the flux of kinetic energy. The wavenumbers shown denote the center wavenumber of the corresponding wavenumber bins, over which the spectral density has been averaged. The bins have a width of  $\pm 66.8 \text{ m}^{-1}$  around the indicated wavenumber location.

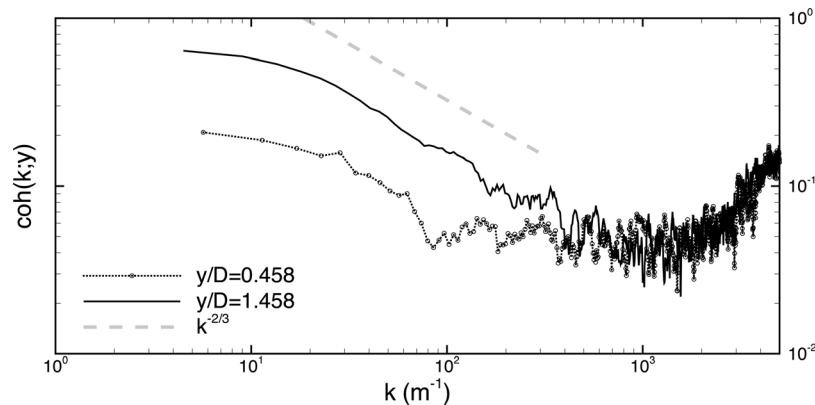


FIG. 16. Coherence spectra at the top and bottom wake locations. The  $\sim k^{-2/3}$  line (Kolmogorov theory) is shown for reference.

and contributions in each bin are averaged. The highest wave number,  $668.5 \text{ m}^{-1}$  (averaged into the  $601.6 \text{ m}^{-1}$  bin), was chosen by consideration of the extent of the inertial subrange of the cospectrum at the bottom of the rotor area, which begins to show significant deviations from the  $-7/3$  at wavenumbers greater than approximately  $700 \text{ m}^{-1}$ . This corresponds to a frequency of about  $1000 \text{ Hz}$ . Dividing this frequency by the freestream velocity,  $9.4 \text{ m/s}$ , determines the upper limit of the wavenumber bin. The largest scales, corresponding to a wavenumber of about  $1 \text{ m}^{-1}$ , are about two orders of magnitude greater in their contribution compared to the other bins, and they show a significant change over the wake area profile, also nearly over an order of magnitude. The results shown in this figure highlight the dominant contribution of large scales of the flow to the vertical flux of kinetic energy. Higher wavenumbers play a smaller role across the entire profile in the wind turbine region. And, very close to the ground, all scales tend to contribute more equally to the total vertical flux of mean kinetic energy.

Figure 16 shows the coherence spectrum at the top and bottom wake regions, for the same downstream location,  $x/D=5$ . The coherence spectra appear to follow the expected classic Kolmogorov scaling of  $k^{2/3}$  at smaller wavenumbers, namely less than  $250 \text{ m}^{-1}$ . At those larger scales, there is a clear order of magnitude difference between the coherence at the top of the wake (at  $y/D=1.46$ ) and bottom of the wake (at  $y/D=0.46$ ). The coherence at the top of the turbine array wake is much larger than the coherence at the bottom wake area, consistent with the higher Reynolds shear stress and Reynolds shear stress correlation coefficient at the top of the wake area. Toward the end of the inertial subrange, at around  $650 \text{ m}^{-1}$ , the difference in coherence between the top and bottom wake locations is no longer significant, and the coherence is very low.

## V. DISCUSSION AND CONCLUSIONS

This wind tunnel experiment has considered the flow structures involved in remediation of the velocity deficit behind a target turbine inside a  $3 \times 3$  model wind turbine array. The study of the flow structures inside turbine arrays aims at better understanding the turbine wake-atmospheric boundary layer interactions that dominate entrainment of mean kinetic energy from the above-wake flow into the wind turbine array. The difference between the fluxes at the top and bottom wake locations creates the net entrainment of kinetic energy available to downstream turbines. This entrainment phenomenon allows subsequent rows of wind turbines to continue to extract energy from the original flow, even in very large wind farms where differences of energy flux in the horizontal direction become negligible. An interesting extension to the current analysis would be to measure the correlations between sweep and ejection events and the power output or loading on the wind turbines, in order to ascertain their impact on unsteady loading. Knowledge of the size of the flow structures, their relative contributions to the net fluxes, and how they are organized could in the future lead to better wind farm designs and

also to a better understanding of the effect of wind farms on the local atmosphere and surface ecosystems. Previous studies<sup>4</sup> have determined the importance of the vertical entrainment of large arrays; the focus here has been on characterizing that entrainment using statistical analysis of flow structures. Data were obtained using hot wire anemometry acquired behind a target turbine inside a  $3 \times 3$  model wind turbine array, in a prior wind tunnel experiment.

Present results show that the vertical entrainment is a large-scale turbulence phenomenon. It is clear from Figure 15 that the (smaller) wavenumbers of around  $60\text{--}70\text{ m}^{-1}$  create the largest difference between the fluxes at the top and bottom of the wake. Using a relationship between length-scale and wavenumber  $\ell \sim 2\pi/k$ , the scales that dominate vertical entrainment of kinetic energy are thus about  $\ell \sim 2\pi/60 \sim 0.1\text{ m}$  or about size of the rotor diameter. Furthermore, the large-scale flow structures show an order of magnitude drop in coherence from the top to the bottom of the wake. This is likely the main cause of the differences in flux at these two locations, where the high level of organization at the top of the wake provides a large downward flux, while the low level of organization at the bottom of the wake reduces the flux out of the wake area. This difference contributes to a net positive entrainment of mean-flow kinetic energy that is then available for extraction at downstream turbines. Part of this energy is of course also dissipated into small-scale turbulence and ultimately into heat.

Quadrant decomposition of the downward flux, as shown in Figure 9, shows ejections and sweeps being the primary contributors to the flux. Outward and inward interactions, quadrants 1 and 3, contribute to decrease the downward entrainment, and they are smaller in magnitude. Sweeps are the greatest component of flux above the turbine wake. Therefore, one can argue that sweeping motions dominate the net entrainment of kinetic energy that can ultimately be used at the wind turbine location. However, within and below the wake, ejections are the greatest contributor, by about 50%. Since the contribution from outward and inward interactions is unchanged over the wake profile, they contribute almost nothing to the net flux. The duration analysis of the quadrant structures within the wake flow is similarly revealing. For stress magnitudes above a representative threshold (e.g.,  $H = 2\text{ (m/s)}^2$ ), ejections and sweeps are both about an order of magnitude larger in relative duration than the other flow structures, and sweeps are slightly of longer duration compared to ejections, making the quadrant 4 events the dominant contributor to eddy duration.

The contribution of each quadrant to the viscous dissipation (or rather its stream-wise experimental surrogate) is an indication of the direct coupling between large and small scales in the turbulence. At the top of the wake area, sweeps and ejections account for 30% and 35% of the viscous dissipation, respectively. The other quadrants 1 and 3 only contribute about 15% each. Therefore, where the dominant momentum and kinetic energy entrainment is taking place, the small scales appear to be directly affected by the large-scales that dominate the fluxes. At the bottom of the wake, each quadrant's contribution is more evenly distributed (contributing nearly 25% each), indicating less dependence of the small scales on the large scales.

Further experimental studies should consider the effects of thermal stratification on the vertical entrainment of kinetic energy and associated flow structures. Applying a stable or unstable thermal profile to the flow may change the size of the eddies contributing to the net flux. Temperature effects may also change the coherence over the profile as the nature of the organized structures, particularly ejections, can change considerably. More significantly, the dependence on large scales of the flow suggests that reduced order analysis of the wake flow may yield further insight. For instance, proper orthogonal decomposition analysis would likely provide further information into the salient features of the flow, as a relatively small number of energetic modes could recapture most of the entrainment characteristics.

## ACKNOWLEDGMENTS

This experiment was funded in part by the NSF (CBET-0730922, CBET-1133800, CBET-0953053). The wind turbine array experiment, during which these data were acquired, was performed in close collaboration with Dr. J. Lebrón-Bosques and Professor L. Castillo. Additional

thanks are extended to Charles Gibson for the aid in developing the data analysis code and compiling the initial results. Their input is gratefully acknowledged.

- <sup>1</sup>S. Frandsen, *J. Wind Eng. Ind. Aerodyn.* **39**, 251 (1992).
- <sup>2</sup>S. Frandsen, R. Barthelmie, S. Pryor, O. Rathmann, S. Larsen, J. Højstrup, and M. Thøgersen, *Wind Energy* **9**, 39 (2006).
- <sup>3</sup>M. Calaf, C. Meneveau, and J. Meyers, *Phys. Fluids* **22**(1), 015110 (2010).
- <sup>4</sup>R. B. Cal, J. Lebron, L. Castillo, H.-S. Kang, and C. Meneveau, *J. Environ. Sustainable Energy* **2**(1), 013106 (2010).
- <sup>5</sup>L. J. Vermeer, J. N. Sørensen, and A. Crespo, "Wind turbine wake aerodynamics," *Prog. Aerosp. Sci.* **39**(6–7), 467–510 (2003).
- <sup>6</sup>P. R. Ebert and D. H. Wood, *Renewable Energy* **18**, 513 (1999).
- <sup>7</sup>P. E. J. Vermeulen, in *Proceedings of the Third International Symposium on Wind Energy Systems* (BHRA Fluid Engineering, England, 1980), Vol. 45, p. 431.
- <sup>8</sup>L. P. Chamorro and F. Porté-Agel, *Boundary-Layer Meteorol.* **132**, 129–149 (2009).
- <sup>9</sup>K. Thomsen and P. Sørensen, *J. Wind Eng. Ind. Aerodyn.* **80**, 121 (1999).
- <sup>10</sup>D. J. Milborrow, *J. Ind. Aerodyn.* **5**, 403 (1980).
- <sup>11</sup>E. A. Bossanyi, G. E. Whittle, P. D. Dunn, N. H. Lipman, P. J. Musgrove, and C. Maclean, in *Proceedings of the Third International Symposium on Wind Energy Systems* (BHRA Fluid Engineering, England, 1980), Vol. 17–44, p. 401.
- <sup>12</sup>M. Magnusson and A. S. Smedman, *J. Wind Eng. Ind. Aerodyn.* **80**, 169 (1999).
- <sup>13</sup>M. Magnusson, *J. Wind Eng. Ind. Aerodyn.* **80**, 147 (1999).
- <sup>14</sup>B. Sanderse, Energy Research Centre of the Netherlands, Report No. ECN-E-09-016, 2009.
- <sup>15</sup>R. J. Barthelmie, K. Hansen, S. T. Frandsen, O. Rathmann, J. G. Schepers, W. Schlez, J. Phillips, K. Rados, A. Zervos, E. S. Politis, and P. K. Chaviaropoulos, *Wind Energy* **12**, 431 (2009).
- <sup>16</sup>Y.-T. Wu and F. Porté-Agel, *Boundary-Layer Meteorol.* **138**, 345 (2011).
- <sup>17</sup>W. W. Willmarth and S. S. Lu, *J. Fluid Mech.* **55**, 65 (1972).
- <sup>18</sup>J. M. Wallace, H. Eckelmann, and R. S. Brodkey, *J. Fluid Mech.* **54**, 39 (1972).
- <sup>19</sup>D. Poggi and G. G. Katul, *Exp. Fluids* **45**, 111–121 (2008).
- <sup>20</sup>Y. Hattori, C.-H. Moeng, H. Suto, N. Tanaka, and H. Hirakuchi, *Boundary-Layer Meteorol.* **134**, 269–283 (2010).
- <sup>21</sup>G. Fabris, *J. Fluid Mech.* **94**, 673 (1979).
- <sup>22</sup>R. A. Antonia and L. W. B. Browne, *Fluid Dyn. Res.* **2**, 3 (1987).
- <sup>23</sup>K. P. Nolan, E. J. Walsh, and D. M. McEligot, *J. Fluid Mech.* **658**, 310–335 (2010).
- <sup>24</sup>M. R. Raupach, *J. Fluid Mech.* **108**, 363 (1981).
- <sup>25</sup>G. Katul, G. Kuhn, J. Schieldge, and C.-I. Hsieh, *Boundary-Layer Meteorol.* **83**, 1 (1997).
- <sup>26</sup>G. Katul, D. Poggi, D. Cava, and J. Finnigan, *Boundary-Layer Meteorol.* **120**, 367 (2006).
- <sup>27</sup>S. Rajagopalan and R. A. Antonia, *Phys. Fluids* **25**, 949–956 (1982).
- <sup>28</sup>D. Lakehal, M. Fulgosi, S. Banerjee, and G. Yadigaroglu, *Phys. Fluids* **20**, 065101 (2008).
- <sup>29</sup>V. Roussinova, A.-M. Shinneeb, and R. Balachandar, *J. Hydraul. Eng.* **136**, 143–154 (2010).
- <sup>30</sup>D. Poggi, A. Porporato, L. Ridolfi, J. Albertson, and G. Katul, *Boundary-Layer Meteorol.* **111**, 565 (2004).
- <sup>31</sup>B. B. Baldocchi and B. A. Hutchison, *Boundary-Layer Meteorol.* **40**, 127 (1987).
- <sup>32</sup>W. Zhu, R. van Hout, and J. Katz, *J. Atmos. Sci.* **64**, 2825 (2007).
- <sup>33</sup>B. B. Baldocchi and T. P. Meyers, *Boundary-Layer Meteorol.* **43**, 345 (1988).
- <sup>34</sup>W. Yue, C. Meneveau, M. B. Parlange, W. Zhu, R. van Hout, and J. Katz, *Water Resour. Res.* **43**, 5422 (2007).
- <sup>35</sup>J. L. Lumley, *Phys. Fluids* **10**, 855 (1967).
- <sup>36</sup>L. Chamorro, R. Arndt, and F. Sotiropoulos, *Wind Energy* **15**, 733 (2012).
- <sup>37</sup>D. Zhu, A. van Hout, L. Luznik, H.-S. Kang, J. Katz, and C. Meneveau, *Exp. Fluids* **41**, 309 (2006).
- <sup>38</sup>J. J. Finnigan, *Boundary-Layer Meteorol.* **16**, 213 (1979).
- <sup>39</sup>H. Tennekes and J. Lumley, *A First Course in Turbulence* (MIT, 1971).
- <sup>40</sup>E. E. Morfiadakis, G. L. Glinou, and M. J. Koulouvari, *J. Wind Eng. Ind. Aerodyn.* **62**, 237 (1996).
- <sup>41</sup>A. Crespo and J. Hernández, *J. Wind Eng. Ind. Aerodyn.* **61**, 71 (1996).
- <sup>42</sup>J. Jiménez, J. C. del Álamo, and O. Flores, *J. Fluid Mech.* **505**, 179 (2004).
- <sup>43</sup>A. Jiménez, A. Crespo, E. Migoya, and J. Garcia, *Environ. Res. Lett.* **3**(1), 015004 (2008).
- <sup>44</sup>G. Comte-Bellot and S. Corrsin, *J. Fluid Mech.* **48**, 273 (1971).
- <sup>45</sup>H.-S. Kang, S. Chester, and C. Meneveau, *J. Fluid Mech.* **480**, 129 (2003).
- <sup>46</sup>S. Emeis, *Wind Energy* **13**, 459 (2010).